Frequency-Independent Terahertz Anomalous Hall Effect in DyCo$_5$, Co$_{32}$Fe$_{68}$, and Gd$_{27}$Fe$_{73}$ Thin Films from DC to 40 THz

Tom S. Seifert,* Ulrike Martens, Florin Radu, Mirkow Ribow, Marco Berritta, Lukáš Nádvorník, Ronald Starke, Tomas Jungwirth, Martin Wolf, Ilie Radu, Markus Münzenberg, Peter M. Oppeneer, Georg Woltersdorf, and Tobias Kampfrath

The anomalous Hall effect (AHE) is a fundamental spintronic charge-to-charge-current conversion phenomenon and closely related to spin-to-charge-current conversion by the spin Hall effect. Future high-speed spintronic devices will crucially rely on such conversion phenomena at terahertz (THz) frequencies. Here, it is revealed that the AHE remains operative from DC up to 40 THz with a flat frequency response in thin films of three technologically relevant magnetic materials: DyCo$_5$, Co$_{32}$Fe$_{68}$, and Gd$_{27}$Fe$_{73}$. The frequency-dependent conductivity-tensor elements σ_{xx} and σ_{yx} are measured, and good agreement with DC measurements is found. The experimental findings are fully consistent with ab initio calculations of σ_{yx} for CoFe and highlight the role of the large Drude scattering rate ($\approx$100 THz) of metal thin films, which smears out any sharp spectral features of the THz AHE. Finally, it is found that the intrinsic contribution to the THz AHE dominates over the extrinsic mechanisms for the Co$_{32}$Fe$_{68}$ sample. The results imply that the AHE and related effects such as the spin Hall effect are highly promising ingredients of future THz spintronic devices reliably operating from DC to 40 THz and beyond.

Incorporating the electron spin into electronic devices is the central idea of spintronics.[1] This growing research field ultimately aims at generating, controlling, and detecting spin currents at terahertz (THz) rates.[2] To realize such high-speed spin operations, spin-orbit interaction (SOI), despite being weak, plays a key role because it couples the motion of an electron to its spin state.[3] From a classical viewpoint, SOI can be understood as a spin-dependent effective magnetic field that deflects copropagating spin-up and spin-down conduction electrons in opposite directions (see **Figure 1**a). Important consequences of SOI are the spin Hall effect (SHE)[4] and its magnetic counterpart, the anomalous Hall effect (AHE).[5,6] In a metal with SOI, the SHE converts a charge current into a transverse pure spin

Dr. T. S. Seifert, Prof. T. Kampfrath, Dr. I. Radu
Department of Physics
Freie Universität Berlin
Berlin 14195, Germany
E-mail: tom.seifert@fu-berlin.de

Dr. T. S. Seifert, Prof. T. Kampfrath, Prof. M. Wolf
Department of Physical Chemistry
Fritz-Haber-Institute of the Max-Planck-Society
Berlin 14195, Germany

Dr. U. Martens, Prof. M. Münzenberg
Institute of Physics
University of Greifswald
Greifswald 17489, Germany

Dr. F. Radu
Helmholtz-Zentrum Berlin für Materialien und Energie
Albert-Einstein-Str. 15, Berlin 12489, Germany

Dr. M. Ribow, Prof. G. Woltersdorf
Institute of Physics
Martin-Luther Universität Halle-Wittenberg
Halle (Saale) 06120, Germany

Dr. M. Berritta,[+] Prof. P. M. Oppeneer
Department of Physics and Astronomy
Uppsala University
P.O. Box 516, Uppsala SE-75120, Sweden

Dr. L. Nádvorník
Faculty of Mathematics and Physics
Charles University
Ke Kalovu 2027/3, Prague 12116, Czech Republic

Dr. R. Starke
TU Bergakademie Freiberg
Freiberg 09599, Germany

Prof. T. Jungwirth
Institute of Physics
Czech Academy of Sciences
Cukrovarnicka 10, Praha 6, 162 00, Czech Republic

Prof. T. Jungwirth
School of Physics and Astronomy
University of Nottingham
Nottingham NG7 2RD, UK

Dr. I. Radu
Max-Born Institute for Nonlinear Optics and Short Pulse Spectroscopy
Max-Born-Str. 2A, Berlin 12489, Germany

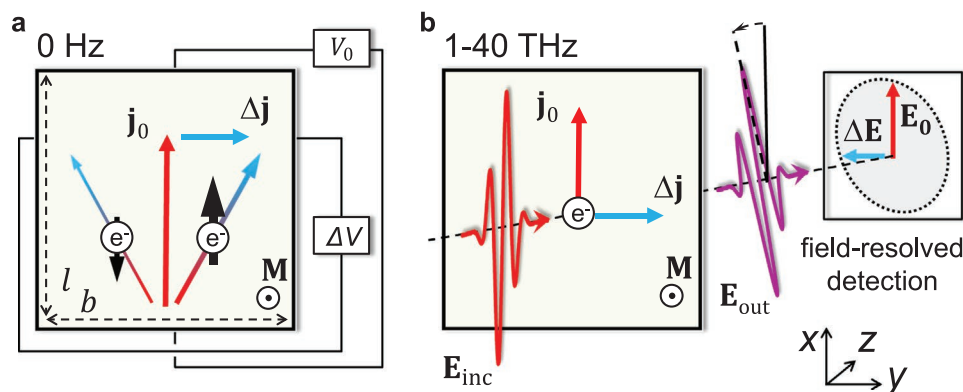The ORCID identification number(s) for the author(s) of this article can be found under https://doi.org/10.1002/adma.202007398.

[+]Present address: College of Engineering, Mathematics and Physical Sciences, University of Exeter, Exeter EX44QL, UK

Figure 1. Schematic of DC and THz anomalous Hall effect measurements. a) In the DC AHE measurement, an applied voltage V_0 drives a DC charge current $\mathbf{j}_0 = j_0\mathbf{u}_x$ parallel to the x axis in a magnetic metallic sample of length l and width b. Spin-orbit interaction (SOI) deflects spin-up and spin-down electrons (black arrows) into opposite directions perpendicular to their velocity and to the sample magnetization $\mathbf{m}\|\mathbf{u}_z$. The different number of majority (spin-up) and minority (spin-down) electrons causes a perpendicular charge current $\Delta\mathbf{j} = \Delta j\mathbf{u}_y$ that leads to a corresponding voltage ΔV measured by a voltmeter. b) In the all-optical AHE measurement, an incident THz electromagnetic pulse with transient electric field $\mathbf{E}_{inc}\|\mathbf{u}_x$ drives an AC charge current $\mathbf{j}_0 = j_0\mathbf{u}_x$ with frequencies from 1 to 40 THz in the plane of the magnetic metal along $\mathbf{E}_{inc}$. SOI induces a transverse charge current $\Delta\mathbf{j} = \Delta j\mathbf{u}_y$, which emits an additional THz electric field component $\Delta\mathbf{E}$ into the optical far-field. The superposition $\mathbf{E}_0 + \Delta\mathbf{E}$ leads to an elliptically polarized THz wave behind the sample. With an electric-field-sensitive detector, both THz polarization components $\mathbf{E}_0$ and $\Delta\mathbf{E}$ are separately measured with femtosecond time resolution.

current. Similarly, the AHE in a ferromagnetic metal causes a transverse spin-polarized charge current proportional to the net magnetization.[7]

Such SOI-induced effects have found broad application in spintronic devices for spin-current generation and detection as well as for switching of magnetic order.[8,9] Up to now, however, most spintronics work has been limited to frequencies below 10 GHz,[10] significantly lagging behind other information carriers such as electrons in field-effect transistors featuring cut-off frequencies of ≈1 THz.[11] Therefore, the question arises how SOI-induced effects evolve at THz frequencies. Previous ultrafast works demonstrated that the inverse SHE is still operative up to 30 THz.[12–21] However, its actual strength, in particular in comparison to low frequencies down to DC, is an open question. Its answer is highly relevant for the transfer of spintronic functionalities to the THz range,[10,22] which can provide access to collective spin dynamics at their natural frequencies, including exchange modes in ferrimagnets[23] and antiferromagnets.[24,25]

From a fundamental viewpoint, studying THz spin-to-charge conversion yields insights into the energetic structure of SOI because the photon energy (4 meV at 1 THz) is comparable to typical SOI energy scales in solids. Since pure spin currents are much more difficult to measure than charge currents, it is reasonable to start with studying the THz AHE. So far, however, no AHE data are available over the entire range from 0 to about 100 meV for magnetic metals relevant to THz spintronics. Notable exceptions are measurements below 6 THz on SrRuO₃[26] magnetic semiconductors,[27,28] and metals.[29,30] For infrared frequencies above 25 THz, again SrRuO₃[31,32] and related compounds were studied.[33]

In this work, we use broadband THz time-domain ellipsometry in combination with DC AHE measurements to extract the complex in-plane conductivity tensor of magnetic metals from 0 to 40 THz, thereby closing the gap between DC and optical frequencies (Figure 1b). A comparison to ab initio

calculations suggests that the large electron scattering rate has two important consequences: First, it makes the THz AHE largely frequency-independent. Second, it reinforces the intrinsic AHE contribution.

We investigate magnetic metals representative of a whole class of materials with large SOI that become increasingly important in ultrafast spintronics: ferromagnetic CoFe[34–36] and the ferrimagnets DyCo₅ and GdFe.[37–39] Their potential ultra-fast applications require characterization and understanding of the spintronic phenomena at accordingly high, that is, THz frequencies. We envisage that our novel broadband THz time-domain ellipsometry does not only allow us to study the presented, technologically highly relevant materials but will also enable studies of the THz spintronic response of emerging material classes in the future.

Conceptual Idea: In our DC AHE measurement (Figure 1a), an electrical voltage drove a spin-polarized current through a magnetic conductor with out-of-plane magnetization. SOI deflected spin-up and spin-down conduction electrons in opposite directions perpendicular to the sample magnetization and the driving current. The resulting transverse spin-polarized anomalous Hall current was measured electrically. Such DC AHE measurements are usually limited to gigahertz frequencies.[40]

To cover the THz frequency range, a quasi-optical and contactless scheme (Figure 1b) was used. A linearly polarized THz electric-field pulse drove a spin-polarized in-plane current in the magnetic metal film. The SOI-induced perpendicular anomalous Hall current emitted THz radiation into the far-field. Consequently, the transmitted THz pulse became elliptically polarized. Using broadband THz time-domain ellipsometry, the driving and induced THz electric field from 1 to 40 THz were measured.

It is noted that the AHE is determined by the same conductivity tensor as the Faraday effect. Thus, the THz AHE measurement can also be considered as the THz Faraday effect, which is a more commonly used term at optical frequencies. Unlike

with optical frequencies, our experimental scheme allows the Drude-response of the spintronically relevant conduction electrons close to the Fermi energy to be studied directly. For photon energies in the mid-infrared region (above ≈ 0.1 eV), however, the free-carrier-like dynamics would be increasingly superimposed by interband transitions.[41]

Materials: Two crystalline (CoFe and $DyCo_5$) and one amorphous (GdFe) material were studied. All samples had an out-of-plane magnetic anisotropy, perfectly suited to achieve large THz AHE signals.

In terms of applications, thin films of CoFeB were proven very useful in magnetic tunnel junctions with up to 500% tunnel-magnetoresistance ratio[42] and for the generation of skyrmion bubbles.[43] They allowed for efficient spin-to-charge-current conversion in double-layer systems[39] and low Gilbert damping.[44] Consequently, CoFeB is one of the leading materials for spintronic applications such as the spin-transfer-torque magnetic random-access memory and magnetic read heads and sensors.[45]

$DyCo_5$ and GdFe belong to the class of ferrimagnetic compounds consisting of rare-earth (RE) and transition-metal (TM) elements. They are interesting for spintronic applications because they exhibit a large SOI, highly tunable magnetic properties and large magnetooptical effects.[46] Another intriguing phenomenon discovered recently on these RE-TM ferrimagnetic alloys is all-optical ultrafast magnetization switching,[47,48] which bears a large potential for magnetic recording.

Sample Characterization: To characterize the magnetic properties of the samples, the Faraday rotation was measured with a continuous-wave laser diode (wavelength of 628 nm) under an angle of incidence of 45° as a function of an external magnetic field oriented normal to the sample plane. The measured square-like hysteresis curve confirmed that the magnetic easy axis was out of the sample plane (see Figure 2b for $DyCo_5$). DC magneto-transport measurements, the results of which are discussed below, were conducted on metallic layers that were patterned into Hall-bar structures (Section S5, Supporting Information). For a complete characterization of the sample's THz conductivity tensor, the THz transmission of the samples

was measured. As a reference, samples were used without metal films as well as only dry air.

Measurement Procedure: In our experiment, the sample magnetization **M** was saturated by an external magnetic field (up to ± 180 mT) and typically switched every 10 s. THz waveforms were averaged over about 1000 cycles. Measurements were performed in remanence, except for the GdFe sample, where an external magnetic field of about ±50 mT was applied owing to the slight nonsquare like hysteresis curve (Sections S1 and S2, Supporting Information). It is emphasized that a 45°-analyzer configuration was employed, which does not require rotation of the THz polarizer. Importantly, this approach is different from the often-used nearly-crossed polarizer-analyzer configurations used in conventional ellipsometry measurements. By not moving any THz optics, systematic errors are minimized arising from, for instance, inhomogeneities of the moving polarizer, which are more pronounced at higher THz frequencies. All measurements were conducted at room temperature in a dry N_2 atmosphere to avoid THz absorption by water vapor.

Raw Data: **Figure 2**a displays the electro-optic signal of THz pulses obtained after transmission through a $DyCo_5$ sample for opposite sample magnetizations. At first glance, that is, on the large scale, the THz signals for magnetization +**M** (red solid curve) and −**M** (black dashed curve) agree almost perfectly. There is, however, a small signal change for opposite magnetizations, which only becomes apparent by magnifying the signal in the vicinity of the maximum at $t = 103$ fs (see inset of Figure 2a). The magnification reveals that switching between the two magnetizations induces signal changes of the order of 2%.

To evaluate these data, we assume the measured signal $S = S_0 + \Delta S$ to be a sum of signals S_0 and ΔS which are, respectively, independent of **M** and linear in **M**. Effects of higher order in **M** are neglected. In this approximation, we obtain

$$S_0 = \frac{S(+\mathbf{M}) + S(-\mathbf{M})}{2} \text{ and } \Delta S = \frac{S(+\mathbf{M}) - S(-\mathbf{M})}{2} \quad (1)$$

By applying this procedure to the waveforms of Figure 2a, we find the magnetization-dependent signal is of the order of
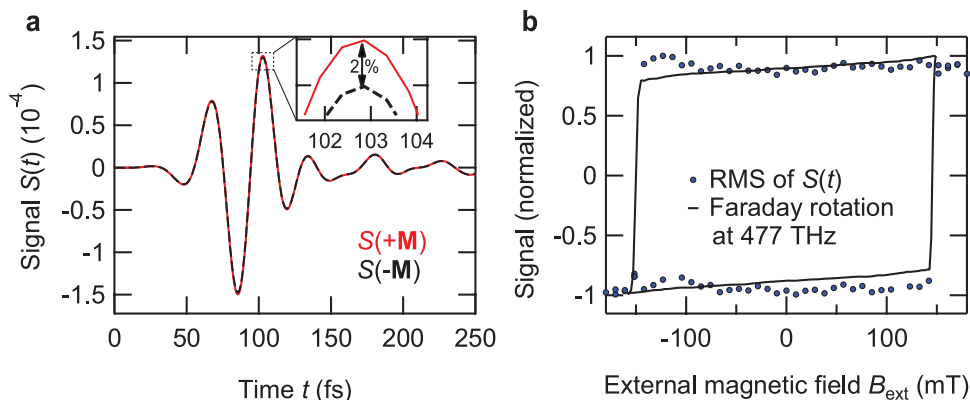

Figure 2. Raw data of the THz AHE of $DyCo_5$. a) THz signal of an initially linearly polarized THz pulse after passing through an out-of-plane magnetized $DyCo_5$ sample. The anomalous Hall effect induces a new perpendicular polarization component, depending on the orientation of the sample magnetization (red solid and black dashed curves). Inset: Magnification reveals a signal change of the order of 2%, suggesting an anomalous Hall angle of similar magnitude. b) Faraday rotation hysteresis curve at optical (628 nm ≙ 477 THz, black solid line) and terahertz (10 to 40 THz, blue circles) frequencies (root mean square (RMS) of the THz waveform $\Delta S(t)$ (Equation (1)), multiplied by its polarity).

**ADVANCED
SCIENCE NEWS**

www.advancedsciencenews.com

**ADVANCED
MATERIALS**

www.advmat.de

$\Delta S/S_0 \approx 2\%$. In addition, $S(+\mathbf{M})$ and $S(-\mathbf{M})$ are almost in phase (Inset of Figure 2a), indicating that the transmitted THz pulse is still linearly polarized.

As a check, we also perform a reference measurement of the bare substrate (150 nm thick Si_3N_4 membrane), which does not result in any detectable signal that depends on the sample magnetization (Figure S1, Supporting Information). To further verify the magnetic origin of the signal, we measure the complete THz waveform as a function of the external magnetic field $\mathbf{B}_{ext}$. Figure 2b shows the root mean square (RMS) of these THz waveforms versus $\mathbf{B}_{ext}$. We find that the THz hysteresis curve follows the optical Faraday rotation hysteresis curve. Therefore, ΔS indeed scales with the sample magnetization.

Conductivity-Tensor Extraction: The signals shown in Figure 2 still depend on sample-extrinsic factors such as the spectrum of the incident THz pulse and the sample substrate. Significantly more information is provided by extracting the conductivity tensor of the metallic magnet from our data. For the analysis, it is sufficient to restrict oneself to the *x*-*y*-plane (Figure 1) because all currents flow in the sample plane. In an isotropic magnetically ordered solid with magnetization $\mathbf{M}\|\mathbf{u}_z$, the current $\mathbf{j}(\omega, z)$ driven by an electric field $\mathbf{E}(\omega, z)$ is at frequency $\omega/2\pi$ and position z given by

$$\mathbf{j} = \underline{\sigma}\,\mathbf{E} = \begin{pmatrix} \sigma_{xx} & -\sigma_{yx} \\ \sigma_{yx} & \sigma_{xx} \end{pmatrix}\mathbf{E} \qquad (2)$$

Here, $\mathbf{E}$ is the electric field inside the sample, and σ_{xx} and σ_{yx} denote the diagonal and off-diagonal conductivity, respectively. Note that the Onsager relations and Equation (2) imply that $\sigma_{yx}(-\mathbf{M}) = \sigma_{xy}(\mathbf{M}) = -\sigma_{yx}(\mathbf{M})$.

The connection to our experiment (Figure 1b) is provided by the Fresnel transmission matrix $\underline{t} = (t_{ij})$, which relates the incident and transmitted electric fields by $\mathbf{E}_{out} = \underline{t}\,\mathbf{E}_{inc}$. Here, the indices i, j equal s or p, which correspond to the x and y axes in a normal-incidence geometry, respectively. In our setup, we do not measure the electric field directly but an electro-optic signal S, which is in the Fourier domain related to the electric field by multiplication with a frequency-dependent setup transfer function. The detector is equally sensitive to s- and p-polarized THz fields because the angle of the THz polarizer behind the sample is set to 45°. By acquiring S for opposite magnetizations $\pm\mathbf{M}$, we obtain the nonmagnetic signal $S_0(\omega)$ and the magnetic signal $\Delta S(\omega)$ (see Equation 1). By taking the ratio, the setup transfer function drops out and we obtain

$$\frac{\Delta S}{S_0} = \frac{\Delta E}{E_0} = \frac{t_{sp}}{t_{pp}} \qquad (3)$$

The coefficient t_{pp} is obtained by an additional reference measurement without sample and using the optical constants for Si_3N_4 as indicated in Table S1 in the Supporting Information.

To approximately determine the information contained in Equation (3), we apply the thin-film approximation.[49] The two Fresnel coefficients for normal incidence become

$$t_{pp}(\omega) = \frac{2n_1(\omega)}{n_1(\omega) + n_2(\omega) + Z_0 G_{xx}(\omega)} \qquad (4)$$

and

$$t_{sp}(\omega) = \frac{t_{pp}^2(\omega)}{2n_1(\omega)} Z_0 G_{yx}(\omega) \qquad (5)$$

where the sheet conductance G_{ij} is given by $G_{ij}(\omega) = \int_0^d dz\,\sigma_{ij}(z,\omega)$, and $Z_0 \approx 377\,\Omega$ is the vacuum impedance. In the special case of frequency-independent optical constants, normal incidence, a homogeneous layer of thickness d between two air half spaces (refractive index $n_1 = n_2 = 1$) and in the limit $Z_0 G_{xx} \ll 1$, one finds $\Delta S/S_0 \approx Z_0 G_{yx}/2$, which is directly proportional to σ_{yx}. The diagonal sheet conductance $G_{xx} = G_{xx}^{FM} + G_{xx}^{Si_3N_4} + G_{xx}^{Ta}$ contains contributions from the Si_3N_4 membrane and from the Ta seed and capping layers. They are measured on individual Si_3N_4 and Si_3N_4|Ta samples, respectively (Section S3, Supporting Information).

Note that the thin-film approximation is valid as long as the metal thickness is much smaller than the THz wavelength and the penetration depth inside the material at the given THz frequency.[12] In metals, the two above characteristic lengths are of the order of 1 μm and 100 nm at 1 THz, respectively.[50] Thus, for the highest THz frequencies, the thin-film approximation becomes inaccurate for metal films with thicknesses in the 10 nm range. Therefore, we employ a more exact transfer-matrix approach instead to extract the in-plane conductivity tensor $\underline{\sigma}$, which also accounts for the 45° angle of incidence of our experiment (Section S4, Supporting Information). **Figures 3** and **4** show the central result of this procedure: the complex-valued conductivity tensor $\underline{\sigma}$ of all studied materials over more than 5 octaves from 1 to 40 THz.

Diagonal Conductivity σ_{xx}: We start with considering the extracted diagonal conductivities σ_{xx} (Figure 3). Note that for DyCo$_5$, we find a good match between DC and THz conductivity. No DC measurements were performed on the other materials.

The frequency-dependence of the conductivity of metals often obeys the Drude formula.[51] It can be derived from the Boltzmann transport equation in the relaxation-time approximation, which considers the conduction electrons as classical particles scattering at the electronic velocity relaxation rate Γ. For all materials, we observe a typical Drude-like behavior, that is, a monotonically decreasing Re σ_{xx} with increasing frequency. By fitting the Drude formula

$$\sigma^{Drude}(\omega) = \frac{\sigma_{DC}}{1 - i\omega/\Gamma} \qquad (6)$$

to our data, we obtain the DC conductivity σ_{DC} and Γ (**Table 1**).

For the extracted average DC conductivity of CoFe(1 nm)|Ta(8 nm), we find good agreement with the value (5×10^5 S m^{-1}) reported[52,53] for pure CoFe. The agreement indicates that the two materials, CoFe and Ta, have a similar conductivity, as also reported previously.[51] To the best of our knowledge, for DyCo$_5$, only one measurement on a much thicker film exists.[54] The conductivity (2.8×10^6 S m^{-1}) is one order of magnitude larger than our result, likely because interface scattering makes a smaller relative contribution to electron
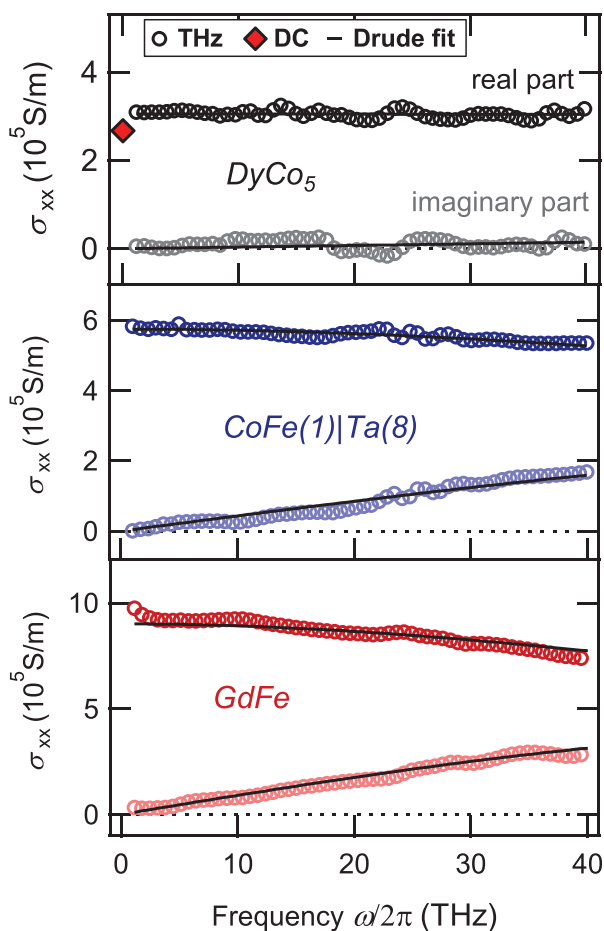
Figure 3. Measured complex-valued diagonal conductivity of DyCo$_5$, CoFe, and GdFe from DC to 40 THz. Diagonal conductivities σ_{xx} measured in the THz frequency range (real part: dark circles, imaginary part: light circles) and at DC (red diamond symbol). For the CoFe sample, only the average conductivity of the CoFe(1 nm)|Ta(8 nm) stack was extracted (see Section S4 in the Supporting Information). Fits (solid lines) were obtained using the Drude model (see Equation (6) and Table 1).

Figure 4. Measured and ab-initio-calculated complex-valued anomalous Hall conductivity of DyCo$_5$, CoFe, and GdFe from DC to 40 THz. Off-diagonal conductivities σ_{yx} measured in the THz frequency range (real part: dark circles, imaginary part: light circles) and at DC (red diamond symbol). Results of ab initio calculations are shown by solid lines for a broadening of $\hbar\gamma = 137$ meV (see Equation (7)). While the orange/yellow lines are the σ_{yx}^{calc} with respect to the external perturbing field (see Equation (8) in the Supporting Information), the green/light-green lines are the conductivity with respect to the external and reaction field (see Equation (9) in the Supporting Information). Experimental errors are estimated from deviations from the condition $\text{Im}\,\sigma_{yx} = 0$ at $\omega = 0$.

scattering in thicker films. However, we find good agreement with the conductivity reported for DyCo$_3$ (3.3 × 10^5 S m^{-1}), the stoichiometry of which is, however, different from our sample.[55] In the case of GdFe, our measured conductivity matches the reported value of 5.0 × 10^5 S m^{-1}.[56,57]

The large current-relaxation rate Γ of more than 100 THz implies that the mean time $1/\Gamma$ between subsequent scattering events amounts to just a few femtoseconds. This observation agrees with previous thin-film studies,[58] which assigned the large scattering rates to strong disorder due, for instance, to small grain sizes and significant interface roughness[59] as well as enhanced electron-phonon scattering in disordered alloys.[60,61]

Off-Diagonal Conductivity σ_{yx}: Figure 4 shows the anomalous Hall conductivity (AHC) extracted from 1 to 40 THz. We note that a small paramagnetic contribution to the signal due to the ordinary Hall effect and slow drifts of the setup may lead to systematic errors, resulting in a nonvanishing value of $\text{Im}\,\sigma_{yx}(\omega = 0)$. Accordingly, the experimental uncertainties are estimated by deviations from the condition $\text{Im}\,\sigma_{yx}(\omega = 0) = 0$. We emphasize
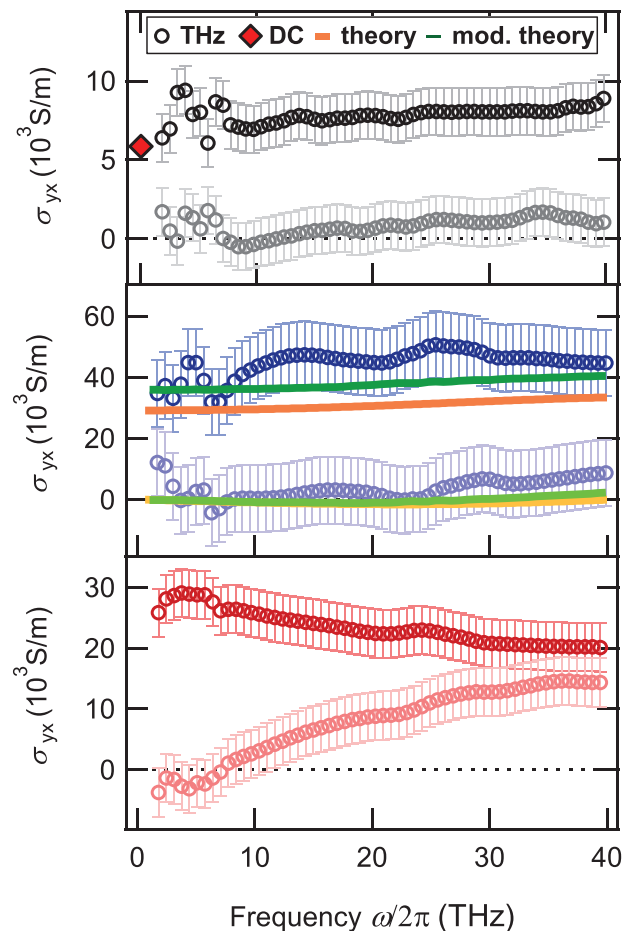
that we again find good agreement between DC and THz measurements. The slightly smaller DC value for DyCo$_5$ may originate from different substrate thicknesses (0.15 vs 500 μm, see Section S5 in the Supporting Information). The good match between DC and THz measurements at the lowest frequencies is not unexpected in view of a variety of recent THz

Table 1. Drude model fit parameters for the experimental diagonal-conductivity data in Figure 3a.

Material	σ_{DC} [10^5 S m^{-1}]	$\Gamma/(2\pi)$ [THz]
DyCo$_5$	3.1	830
CoFe(1 nm) Ta(8 nm)	5.8	130
GdFe	9.0	100
Ta (see Section S2 in the Supporting Information)	5.7	130

spintronic studies.[12,62–64] In comparison to reported values, we find good agreement for GdFe (2.5×10^4 S m^{-1}).[54] For DyCo$_5$, the values reported[52] for much thicker films are 3 times larger (3.3×10^4 S m^{-1}). For CoFe, our measured AHC agrees well with ab initio calculation of the intrinsic AHC (3.3×10^4 S m^{-1}).[65]

We find that Reσ_{yx} only slightly changes toward low THz frequencies (Figure 4), whereas Imσ_{yx} exhibits an approximately linear decrease toward low frequencies. This behavior is consistent with the fact that Reσ_{yx} is even with respect to ω, whereas Imσ_{yx} is odd, because the conductivity is a real-valued quantity in the time domain. Notably, the overall spectral behavior of σ_{yx} is qualitatively analogous to σ_{xx}.

Intrinsic AHE Contribution: To discuss the frequency dependence of the measured σ_{yx} (Figure 4), we first review the microscopic mechanisms that contribute to the AHE: (i) The intrinsic contribution, which is already present in a perfect crystal, and the extrinsic mechanisms (ii) skew scattering and (iii) side jump.[4–6]

In many theoretical considerations in the DC limit,[5,6] the intrinsic contribution (i) is often discussed in terms of the anomalous velocity, which is a velocity component perpendicular to the driving electric field. The anomalous velocity scales linearly with the instantaneous value of the driving electric field and the real-valued Berry curvature, which results in a conductivity component σ_{yx} that is independent of frequency along with Im$\sigma_{yx} = 0$. This notion does not agree with our observations: For GdFe, for instance, σ_{yx} changes strongly with frequency (Figure 4). In particular, Imσ_{yx} increases with frequency.

We note that the concept of the anomalous velocity is only valid at sufficiently low frequencies of the driving field.[5] At arbitrary frequencies, the AHE can be calculated within Kubo linear-response theory using[66]

$$\sigma_{yx}^{\text{calc}}(\omega) = \frac{ie^2\hbar}{m^2 V} \sum_{\mathbf{k},n,n'} \frac{f(\varepsilon_{\mathbf{k}n}) - f(\varepsilon_{\mathbf{k}n'})}{\varepsilon_{\mathbf{k}n} - \varepsilon_{\mathbf{k}n'}} \frac{\langle \mathbf{k}n'| \hat{\mathbf{p}}_y |\mathbf{k}n\rangle \langle \mathbf{k}n| \hat{\mathbf{p}}_x |\mathbf{k}n'\rangle}{\varepsilon_{\mathbf{k}n'} - \varepsilon_{\mathbf{k}n} + \hbar\omega + i\hbar\gamma} \quad (7)$$

Here, the involved quantities are the matrix elements of the momentum operator $\hat{\mathbf{p}}$, the Bloch band energies $\varepsilon_{\mathbf{k}n}$, initial and final Bloch states $|\mathbf{k}n\rangle$ and $|\mathbf{k}n'\rangle$, the system volume V, the electron mass m, and the Fermi–Dirac function $f(\varepsilon_{\mathbf{k}n})$. In the limit $\omega \to 0$ and $\gamma \to 0$, Equation (7) leads to the frequently used expression for the DC AHC in terms of the Berry curvature.[5]

Our calculations, differently from those presented in ref. [67], also introduce the effect of the Bloch electrons' lifetimes quantified by the inverse lifetime γ of the state. We note that even though this spectral broadening is introduced phenomenologically, a suitable range of values is known for metals.[61] For transitions near the Fermi energy, γ is expected to be of the same order as the relaxation rate Γ of the Drude formula (see Equation (6)).

The summation over the band indices n, n' and wavevectors $\mathbf{k}$ accounts for all allowed transitions. The Bloch states, band energies, and momentum matrix elements are computed using a relativistic density-functional theory implementation.[68] Note that the contribution from intraband transitions ($n = n'$) in Equation (7) is zero, in contrast to the diagonal tensor element
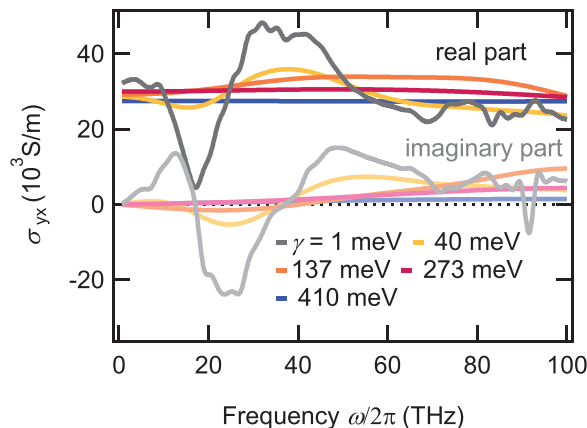

Figure 5. Ab initio calculated anomalous Hall conductivity. Theoretical off-diagonal conductivity $\sigma_{yx}^{\text{calc}}$ of CoFe calculated for different broadenings according to Equation (7). The light-colored lines are the respective imaginary parts.

$\sigma_{xx}(\omega)$, where the intraband contribution leads to a Drude-like conductivity. The $\sigma_{xx}(\omega)$ can in principle be computed ab initio, but it strongly depends on the details of the sample quality and is, thus, not done here.

The calculated $\sigma_{yx}^{\text{calc}}$ are shown in **Figure 5** from 0 to 100 THz for various choices of γ. For $\hbar\gamma = 137$ meV, we find good agreement with the complex-valued measured σ_{yx} (see Figure 4 for CoFe). This observation is consistent with the expectation $\gamma = \Gamma/2$, which can be derived by comparison of the Drude and the Kubo formula (Equation (6) and (7)). The substantial frequency dependence of $\sigma_{yx}^{\text{calc}}$ arises from resonant interband transitions for which $\varepsilon_{\mathbf{k}n'} - \varepsilon_{\mathbf{k}n} + \hbar\omega \approx 0$ in Equation (7). These spectral features are particularly pronounced for smaller values of γ (Figure 5). Similar observations were reported for SrRuO$_3$ at temperatures at about 10 K and frequencies of around 1 THz.[26]

In contrast, our measured frequency dependence is featureless (Figure 4). Comparison with the ab initio computed AHC suggests that the flat frequency response of σ_{yx} arises from the large scattering rate of the electrons. The large value of γ leads to a significant broadening of electronic transitions underlying the AHE and so smears out sharp spectral features of σ_{yx} that can be observed for the smallest broadening in Figure 5.

External versus Proper Conductivity: We note that the conductivity calculated by the Kubo formalism (see Equation (7)) is called external (likewise direct or full) conductivity because it relates the external (incident) electric field to the current driven inside the sample. In contrast, the measured conductivity refers to the total electric field **E** (incident plus reaction field) inside the sample (Equation (2)).[69] It is called proper conductivity.

To account for this effect (Section S7, Supporting Information), we multiply the calculated external off-diagonal conductivity $\sigma_{yx}^{\text{calc}}$ by $(1 + Z_0\sigma_{xx}d/2)^2$, as shown in Figure 4 (dark and light green curves) and in Figure S4 (Supporting Information) for other broadenings. While the agreement of experiment and theory for Im$\sigma_{yx}(\omega)$ remains effectively the same, it has improved noticeably for Re$\sigma_{yx}(\omega)$. We conclude that the intrinsic AHE mechanism can well explain the measured

proper $\sigma_{yx}(\omega)$ of CoFe, both in terms of magnitude and frequency dependence, provided a sufficient lifetime broadening is introduced. Even better agreement is obtained when one accounts for the fact that the calculated conductivity (Equation (7)) is the external conductivity.

The observed discrepancy between theory and experiment of only about 20% may arise from extrinsic contributions to the AHE, the different stoichiometries employed for CoFe in the experiment and in the calculation (see Section S6 in the Supporting Information) as well as substrate-induced stress in the thin metal films, all of which are neglected in the calculations.

Extrinsic AHE Contributions: We note that in Equation (7), Bloch states are assumed to be the single-particle states for the electrons of the unperturbed system. The extrinsic AHE contributions skew scattering (ii) and side-jump[5,6] (iii) are neglected. In the following, we estimate the strength of (ii) and (iii).

For the skew-scattering contribution (ii), we employ a simple Boltzmann-equation-type model (Section S8, Supporting Information). The resulting dependence on frequency (but not on Γ) is identical to that of the ordinary Hall effect (see Equation (23) in the Supporting Information): We find the Drude-type relationship of Equation (6) for σ_{xx}, whereas $\sigma_{yx}^{sk}(\omega) \propto (1 - i\omega/\Gamma)^{-2} \approx (1 - 2i\omega/\Gamma)^{-1}$. Therefore, the normalized imaginary part $\text{Im}\,\sigma_{yx}^{sk}(\omega)/\sigma_{xy}(0)$ of the skew-scattering component should increase with slope $(2/\Gamma)\sigma_{yx}^{sk}(0)/\sigma_{yx}(0)$.

To obtain an upper limit of the skew-scattering contribution for CoFe, we assume that the measured slope of $\text{Im}\,\sigma_{yx}(\omega)$ exclusively arises from skew scattering. We obtain $\sigma_{yx}^{sk}(0)/\sigma_{yx}(0) < 0.3$, that is, skew scattering would at most contribute about 30% to the AHC. In this estimate, we assumed similar values of Γ for CoFe and Ta in the CoFe(1 nm)|Ta(8 nm) bilayer as justified by measurements of $\sigma_{xx}(\omega)$ in pure Ta films (Table 1; Figure S2, Supporting Information). This result is in line with previous notions[5] that the low conductivity of our sample places it in the bad-metal regime. There, skew-scattering is known to make a rather negligible contribution to σ_{yx}, and the intrinsic mechanism dominates.

Concerning the side-jump component (iii), we note that its contribution is difficult to discriminate against the intrinsic contribution.[5] However, side-jump is typically one order of magnitude weaker than the intrinsic contribution.[68]

To summarize, the good agreement of our calculations based on Equation (7) with the measured data (Figure 4) and the estimated small magnitude of less than 25% of the skew-scattering contribution strongly suggest that the intrinsic mechanism dominates σ_{yx} at least for CoFe. This conclusion appears reasonable because the intrinsic contribution is enhanced by the large SOI of d-electrons around the Fermi energy, as in our samples. Thus, the large quasiparticle scattering rate in our samples has two important consequences: It suppresses the extrinsic skew-scattering contribution, and it smears out any spectral feature in σ_{yx}.

Anomalous Hall Angle: We finally consider the anomalous Hall angle (AHA), which is defined as $\Theta_{AH}(\omega) = \sigma_{yx}(\omega)/\sigma_{xx}(\omega) = \Delta j(\omega)/j_0(\omega)$ and displayed for DyCo$_5$ and GdFe in **Figure 6**. The Θ_{AH} of CoFe could not be determined because its σ_{xx} could not be separated from that of Ta in the CoFe|Ta
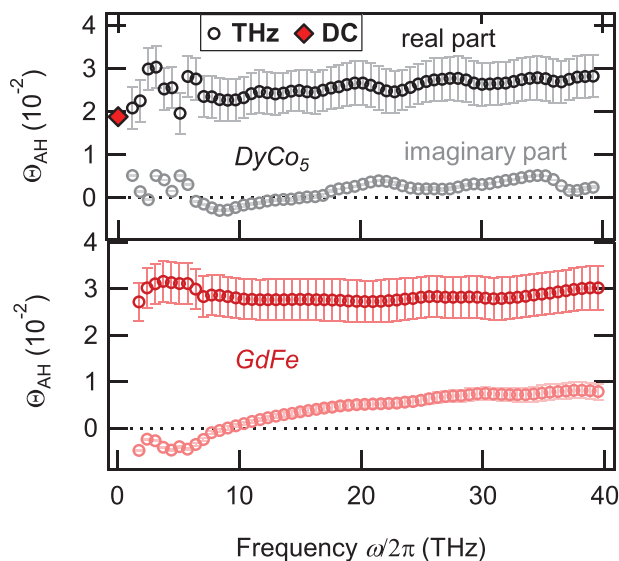

Figure 6. Measured complex-valued THz anomalous Hall angles of DyCo$_5$ and GdFe. Anomalous Hall angles Θ_{AH} measured in the THz frequency range (real part: dark circles, imaginary part: light circles) and at DC (red diamond symbol). Experimental errors are estimated from the uncertainty in σ_{yx} (see Figure 4).

sample. We find a largely frequency-independent Θ_{AH} from DC to 40 THz with frequency-averaged values of 2.6% for DyCo$_5$ and 2.9% for GdFe (Figure 6). The THz AHA of DyCo$_5$ approximately agrees with its measured DC value of 2%. Note that the driving and the AHE-induced electric field components, i.e., ΔE and E_0, are in phase (Figure 2a), already indicating a real-valued AHA for DyCo$_5$. Indeed, in the electrostatic limit, one has $\Delta E/E_0 = \text{Re}\,\Theta_{AH} \approx 2\%$ (Section S5, Supporting Information), consistent with the raw data in Figure 2a. We find good agreement between our measured AHA values and reported values for GdFe (2.5% in ref. [70] and 4% in ref. [71]). We are not aware of any reported Θ_{AH} for DyCo$_5$.

For DyCo$_5$, $\text{Im}\,\Theta_{AH}$ is relatively small for all frequencies, whereas for GdFe, $\text{Im}\,\Theta_{AH}$ monotonically increases with ω up to 30% of $\text{Re}\,\Theta_{AH}$ at 40 THz. The positive slope of $\text{Im}\,\Theta_{AH}(\omega)$ implies that the AHE-induced current Δj lags behind the primary current j_0 (Figure 1) by the group delay $\partial \arg\Theta_{AH}(\omega)/\partial\omega \approx 1.2$ fs. Therefore, in our experimental frequency range, the bandwidth of σ_{yx} is smaller than the bandwidth of σ_{xx}, which is of the order of Γ. A possible reason for the reduced bandwidth of σ_{yx} is suggested by Equation (7): Bloch states with strong SOI exist only in a limited energy range significantly smaller than $\hbar\Gamma$ around the Fermi energy. Thus, only transitions with frequencies $|\omega|$ significantly below Γ contribute to the sum of Equation (7).

Conclusion: In summary, we developed a technique to measure the AHE in metals continuously from DC to 40 THz, which is a highly relevant spectral window with respect to SOI energy scales. In the studied materials, the AHE is operative even at the highest THz frequencies. For DyCo$_5$, we explicitly confirmed the consistency of our high-frequency with DC measurements. The quantitative agreement with ab initio calculations for CoFe leads us to the conclusion that the intrinsic AHE contribution dominates and that the spectrally flat

off-diagonal conductivity originates from the large quasi-particle scattering rates.

Since the intrinsic contribution to the SHE and the AHE share the same physical origin at zero frequency, the Berry curvature,[4] our results strongly suggest that also the intrinsic SHE contribution of metals is largely frequency-independent up to 40 THz. This conclusion agrees with calculations of the SHE conductance of Pt and W, which found a constant value up to about 100 THz.[72] Our study, thus, closes the gap between DC and the THz range for both AHE and SHE.

Future studies based on our methodology will permit even more insight into SOI at THz frequencies. More pronounced spectral features in the AHC are theoretically expected for samples with small broadening. Experimentally, such reduced level broadening can be achieved by either measuring at low temperatures[33,73] or by using samples with fewer impurities. In principle, we see no obstacle to employ our broadband technique at low temperatures. As Kim et al.[33] showed, a direct distinction between extrinsic and intrinsic contributions to the AHE conductivity becomes possible if $\Gamma/2\pi$ lies in the experimentally covered frequency window.[21] This case is especially interesting for systems with similar-sized intrinsic and extrinsic effects at DC such as L1$_0$ FePt.[74] Finally, extending this measurement scheme to nonmagnetic materials by means of spin injection will allow one to all-optically observe the dynamics of the SHE.[17]

Experimental Section

Materials: The ferromagnetic $Co_{20}Fe_{60}B_{20}$ film with the layer stacking MgO(2 nm)|$Co_{20}Fe_{60}B_{20}$(1 nm)|Ta(8 nm)‖Si_3N_4(150 nm) was prepared by magnetron sputtering and electron-beam evaporation (see Section S3 in the Supporting Information). The Fe-rich composition of CoFeB was chosen to ensure, on one hand, an out-of-plane magnetic anisotropy even at a thickness as large as 1 nm.[75] On the other hand, the Co content enhanced the magnetic moment and, thus, the AHE signal. As prepared, $Co_{20}Fe_{60}B_{20}$ grew extremely smooth because of the B content and its amorphous nature. Post-growth annealing at 300 °C triggered diffusion of the B atoms into the Ta buffer layer, and CoFe crystallization was initiated from the MgO interface. The MgO|CoFe interface was known to exhibit an exceptionally high out-of-plane magnetic anisotropy after crystallization.[75] Because of the lack of boron after annealing, the CoFeB films are denoted as CoFe in the main text.

Ferrimagnetic $Gd_{27}Fe_{73}$ and $DyCo_5$ alloys were grown by magnetron sputtering with the following stacking sequence: Ta(3 nm)|X(20 nm)|Ta(5 nm)‖Si_3N_4(150 nm) with X being either $Gd_{27}Fe_{73}$ or $DyCo_5$ (see Section S3 in the Supporting Information). Both systems have a remanence magnetization state close to saturation magnetization (see Figure 1 and ref. [77]). The chosen composition of $Gd_{27}Fe_{73}$ and $DyCo_5$ ensured an out-of-plane magnetic anisotropy and a magnetization compensation temperature that was far above[77] ($DyCo_5$) or below[78] ($Gd_{27}Fe_{73}$) the measurement temperature (300 K). The coercive magnetic fields could be reached with moderate external magnetic-field strengths, which were limited to about 150 mT in the experiment. In the main text, we refer to $Gd_{27}Fe_{73}$ as GdFe for brevity.

Supporting Information

Supporting Information is available from the Wiley Online Library or from the author.

Conflict of Interest

The authors declare no conflict of interest.

Data Availability Statement

The data that support the findings of this study are available from the corresponding author upon reasonable request.

[1] E. Y. Vedmedenko, R. K. Kawakami, D. D. Sheka, P. Gambardella, A. Kirilyuk, A. Hirohata, C. Binek, O. Chubykalo-Fesenko, S. Sanvito, B. J. Kirby, J. Grollier, K. Everschor-Sitte, T. Kampfrath, C. Y. You, A. Berger, *J. Phys. D: Appl. Phys.* **2020**, *53*, 453001.

[2] J. Walowski, M. Münzenberg, *J. Appl. Phys.* **2016**, *120*, 140901.

[3] A. Manchon, H. C. Koo, J. Nitta, S. M. Frolov, R. A. Duine, *Nat. Mater.* **2015**, *14*, 871.

[4] J. Sinova, S. O. Valenzuela, J. Wunderlich, C. H. Back, T. Jungwirth, *Rev. Mod. Phys.* **2015**, *87*, 1213.

[5] N. Nagaosa, J. Sinova, S. Onoda, A. H. Macdonald, N. P. Ong, *Rev. Mod. Phys.* **2010**, *82*, 1539.

[6] N. A. Sinitsyn, *J. Phys.: Condens. Matter* **2008**, *20*, 023201.

[7] V. P. Amin, J. Li, M. D. Stiles, P. M. Haney, *Phys. Rev. B* **2019**, *99*, 220405.

[8] I. M. Miron, K. Garello, G. Gaudin, P.-J. Zermatten, M. V. Costache, S. Auffret, S. Bandiera, B. Rodmacq, A. Schuhl, P. Gambardella, *Nature* **2011**, *476*, 189.

[9] P. Wadley, B. Howells, J. Elezny, C. Andrews, V. Hills, R. P. Campion, V. Novak, K. Olejnik, F. Maccherozzi, S. S. Dhesi, S. Y. Martin,

**ADVANCED
SCIENCE NEWS**

www.advancedsciencenews.com

**ADVANCED
MATERIALS**

www.advmat.de

T. Wagner, J. Wunderlich, F. Freimuth, Y. Mokrousov, J. Kune, J. S. Chauhan, M. J. Grzybowski, A. W. Rushforth, K. W. Edmonds, B. L. Gallagher, T. Jungwirth, *Science* **2016**, *351*, 587.

[10] E. Y. Vedmedenko, R. K. Kawakami, D. D. Sheka, P. Gambardella, A. Kirilyuk, A. Hirohata, C. Binek, O. Chubykalo-Fesenko, S. Sanvito, B. J. Kirby, J. Grollier, K. Everschor-Sitte, T. Kampfrath, C.-Y. You, A. Berger, *J. Phys. D: Appl. Phys.* **2020**, *53*, 453001.

[11] J. A. Del Alamo, *Nature* **2011**, *479*, 317.

[12] T. Seifert, S. Jaiswal, U. Martens, J. Hannegan, L. Braun, P. Maldonado, F. Freimuth, A. Kronenberg, J. Henrizi, I. Radu, E. Beaurepaire, Y. Mokrousov, P. M. Oppeneer, M. Jourdan, G. Jakob, D. Turchinovich, L. M. Hayden, M. Wolf, M. Münzenberg, M. Kläui, T. Kampfrath, *Nat. Photonics* **2016**, *10*, 483.

[13] T. Seifert, S. Jaiswal, M. Sajadi, G. Jakob, S. Winnerl, M. Wolf, M. Kläui, T. Kampfrath, *Appl. Phys. Lett.* **2017**, *110*, 252402.

[14] T. Seifert, U. Martens, S. Günther, M. A. W. Schoen, F. Radu, X. Z. Chen, I. Lucas, R. Ramos, M. H. Aguirre, P. A. Algarabel, A. Anadón, H. S. Körner, J. Walowski, C. Back, M. R. Ibarra, L. Morellón, E. Saitoh, M. Wolf, C. Song, K. Uchida, M. Münzenberg, I. Radu, T. Kampfrath, *SPIN* **2017**, *07*, 1740010.

[15] Y. Wu, M. Elyasi, X. Qiu, M. Chen, Y. Liu, L. Ke, H. Yang, *Adv. Mater.* **2017**, *29*, 1603031.

[16] D. Yang, J. Liang, C. Zhou, L.u Sun, R. Zheng, S. Luo, Y. Wu, J. Qi, *Adv. Opt. Mater.* **2016**, *4*, 1944.

[17] L. K. Werake, B. A. Ruzicka, H. Zhao, *Phys. Rev. Lett.* **2011**, *106*, 107205.

[18] Y. Sasaki, K. Z. Suzuki, S. Mizukami, *Appl. Phys. Lett.* **2017**, *111*, 102401.

[19] G. Torosyan, S. Keller, L. Scheuer, R. Beigang, E. T. Papaioannou, *Sci. Rep.* **2018**, *8*, 1311.

[20] T. J. Huisman, C. Ciccarelli, A. Tsukamoto, R. V. Mikhaylovskiy, Th. Rasing, A. V. Kimel, *Appl. Phys. Lett.* **2017**, *110*, 072402.

[21] S. Priyadarshi, K. Pierz, M. Bieler, *Phys. Rev. Lett.* **2015**, *115*, 257401.

[22] T. S. Seifert, S. Jaiswal, J. Barker, S. T. Weber, I. Razdolski, J. Cramer, O. Gueckstock, S. F. Maehrlein, L. Nadvornik, S. Watanabe, C. Ciccarelli, A. Melnikov, G. Jakob, M. Münzenberg, S. T. B. Goennenwein, G. Woltersdorf, B. Rethfeld, P. W. Brouwer, M. Wolf, M. Kläui, T. Kampfrath, *Nat. Commun.* **2018**, *9*, 2899.

[23] S. Wienholdt, D. Hinzke, U. Nowak, *Phys. Rev. Lett.* **2012**, *108*, 247207.

[24] T. Kampfrath, A. Sell, G. Klatt, A. Pashkin, S. Mährlein, T. Dekorsy, M. Wolf, M. Fiebig, A. Leitenstorfer, R. Huber, *Nat. Photonics* **2011**, *5*, 31.

[25] K. Olejník, T. Seifert, Z. Kašpar, V. Novák, P. Wadley, R. P. Campion, M. Baumgartner, P. Gambardella, P. Němec, J. Wunderlich, J. Sinova, P. Kužel, M. Müller, T. Kampfrath, T. Jungwirth, *Sci. Adv.* **2018**, *4*, eaar3566.

[26] R. Shimano, Y. Ikebe, K. S. Takahashi, M. Kawasaki, N. Nagaosa, Y. Tokura, *Europhys. Lett.* **2011**, *95*, 17002.

[27] T. J. Huisman, R. V. Mikhaylovskiy, A. V. Telegin, Y.u P. Sukhorukov, A. B. Granovsky, S. V. Naumov, Th. Rasing, A. V. Kimel, *Appl. Phys. Lett.* **2015**, *106*, 132411.

[28] K. N. Okada, Y. Takahashi, M. Mogi, R. Yoshimi, A. Tsukazaki, K. S. Takahashi, N. Ogawa, M. Kawasaki, Y. Tokura, *Nat. Commun.* **2016**, *7*, 12245.

[29] T. J. Huisman, R. V. Mikhaylovskiy, Th. Rasing, A. V. Kimel, A. Tsukamoto, B. De Ronde, L. Ma, W. J. Fan, S. M. Zhou, *Phys. Rev. B* **2017**, *95*, 094418.

[30] T. Matsuda, N. Kanda, T. Higo, N. P. Armitage, S. Nakatsuji, R. Matsunaga, *Nat. Commun.* **2020**, *11*, 909.

[31] M.-H. Kim, G. Acbas, M.-H. Yang, I. Ohkubo, H. Christen, D. Mandrus, M. A. Scarpulla, O. D. Dubon, Z. Schlesinger, P. Khalifah, J. Cerne, *Phys. Rev. B* **2007**, *75*, 214416.

[32] M.-H. Kim, G. Acbas, M.-H. Yang, M. Eginligil, P. Khalifah, I. Ohkubo, H. Christen, D. Mandrus, Z. Fang, J. Cerne, *Phys. Rev. B* **2010**, *81*, 235218.

[33] M.-H. Kim, T. Tanaka, C. T. Ellis, A. Mukherjee, G. Acbas, I. Ohkubo, H. Christen, D. Mandrus, H. Kontani, J. Cerne, *Phys. Rev. B* **2013**, *88*, 155101.

[34] I. Radu, K. Vahaplar, C. Stamm, T. Kachel, N. Pontius, H. A. Dürr, T. A. Ostler, J. Barker, R. F. L. Evans, R. W. Chantrell, A. Tsukamoto, A. Itoh, A. Kirilyuk, Th. Rasing, A. V. Kimel, *Nature* **2011**, *472*, 205.

[35] A. Kirilyuk, A. V. Kimel, T. Rasing, *Rev. Mod. Phys.* **2010**, *82*, 2731.

[36] S. Mangin, M. Gottwald, C. - H. Lambert, D. Steil, V. Uhlíř, L. Pang, M. Hehn, S. Alebrand, M. Cinchetti, G. Malinowski, Y. Fainman, M. Aeschlimann, E. E. Fullerton, *Nat. Mater.* **2014**, *13*, 286.

[37] S. Ikeda, K. Miura, H. Yamamoto, K. Mizunuma, H. D. Gan, M. Endo, S. Kanai, J. Hayakawa, F. Matsukura, H. Ohno, *Nat. Mater.* **2010**, *9*, 721.

[38] S. Baumann, F. Donati, S. Stepanow, S. Rusponi, W. Paul, S. Gangopadhyay, I. G. Rau, G. E. Pacchioni, L. Gragnaniello, M. Pivetta, J. Dreiser, C. Piamonteze, C. P. Lutz, R. M. Macfarlane, B. A. Jones, P. Gambardella, A. J. Heinrich, H. Brune, *Phys. Rev. Lett.* **2015**, *115*, 237202.

[39] L. Liu, C.-F. Pai, Y. Li, H. W. Tseng, D. C. Ralph, R. A. Buhrman, *Science* **2012**, *336*, 555.

[40] D. Wei, M. Obstbaum, M. Ribow, C. H. Back, G. Woltersdorf, *Nat. Commun.* **2014**, *5*, 3768.

[41] T. Kampfrath, L. Perfetti, F. Schapper, C. Frischkorn, M. Wolf, *Phys. Rev. Lett.* **2005**, *95*, 187403.

[42] Y. M. Lee, J. Hayakawa, S. Ikeda, F. Matsukura, H. Ohno, *Appl. Phys. Lett.* **2007**, *90*, 212507.

[43] W. Jiang, P. Upadhyaya, W. Zhang, G. Yu, M. B. Jungfleisch, F. Y. Fradin, J. E. Pearson, Y. Tserkovnyak, K. L. Wang, O. Heinonen, S. G. E. Te Velthuis, A. Hoffmann, *Science* **2015**, *349*, 283.

[44] B. Lenk, H. Ulrichs, F. Garbs, M. Münzenberg, *Phys. Rep.* **2011**, *507*, 107.

[45] Editorial, *Nat. Nanotechnol* **2015**, *10*, 185.

[46] F. Radu, J. Sánchez-Barriga, *Novel Magnetic Nanostructures*, Elsevier, Amsterdam, The Netherlands **2018**, pp. 267–331.

[47] C. D. Stanciu, F. Hansteen, A. V. Kimel, A. Kirilyuk, A. Tsukamoto, A. Itoh, Th. Rasing, *Phys. Rev. Lett.* **2007**, *99*, 047601.

[48] K. Carva, P. Baláž, I. Radu, *Handbook of Magnetic Materials* (Ed: E. Bruck), Vol. *26*, Elsevier, Amsterdam, The Netherlands **2017**, pp. 291–463.

[49] L. Mills, *Nonlinear Optics: Basic Concepts*, Springer Science & Business Media, Berlin, Germany **2012**.

[50] M. A. Ordal, L. L. Long, R. J. Bell, S. E. Bell, R. R. Bell, R. W. Alexander, C. A. Ward, *Appl. Opt.* **1983**, *22*, 1099.

[51] M. Dressel, M. Scheffler, *Ann. Phys. (Leipzig)* **2006**, *15*, 535.

[52] S. B. Wu, T. Zhu, X. F. Yang, S. Chen, *J. Appl. Phys.* **2013**, *113*, 17C717.

[53] M. Cecot, Ł. Karwacki, W. Skowroński, J. Kanak, J. Wrona, A. Żywczak, L. Yao, S. Van Dijken, J. Barnaś, T. Stobiecki, *Sci. Rep.* **2017**, *7*, 968.

[54] V. F. Bochkarev, V. A. Buravikhin, V. T. Sukhomlin, V. A. Egorov, *Russ. Phys. J.* **1973**, *16*, 1753.

[55] P. de V. Du Plessis, T. Germishuyse, *J. Magn. Magn. Mater.* **1992**, *104–107*, 1349.

[56] S. Honda, M. Nawate, M. Ohkoshi, T. Kusuda, *J. Appl. Phys.* **1985**, *57*, 3204.

[57] T. Hauet, F. Montaigne, M. Hehn, Y. Henry, S. Mangin, *Phys. Rev. B* **2009**, *79*, 224435.

[58] K. L. Krewer, W. Zhang, J. Arabski, G. Schmerber, E. Beaurepaire, M. Bonn, D. Turchinovich, *Appl. Phys. Lett.* **2020**, *116*, 102406.

[59] K. Fuchs, *Math. Proc. Cambridge Philos. Soc.* **1938**, *34*, 100.

[60] R. N. Jana, A. K. Meikap, *Phys. Lett. A* **2018**, *382*, 984.

[61] J. J. Lin, C. Y. Wu, *Europhys. Lett.* **1995**, *29*, 141.

[62] J. Cramer, T. Seifert, A. Kronenberg, F. Fuhrmann, G. Jakob, M. Jourdan, T. Kampfrath, M. Kläui, *Nano Lett.* **2018**, *18*, 1064.

[63] M. Meinert, B. Gliniors, O. Gueckstock, T. S. Seifert, L. Liensberger, M. Weiler, S. Wimmer, H. Ebert, T. Kampfrath, *Phys. Rev. Appl.* **2020**, *14*, 064011.

[64] L. Nadvorník, M. Borchert, L. Brandt, R. Schlitz, K. A. de Mare, K. Výborný, I. Mertig, G. Jakob, M. Kläui, S. T. B. Goennenwein, M. Wolf, G. Woltersdorf, M. Wolf, T. Kampfrath, arXiv:2010.06280, **2020**.

[65] K. M. Seemann, F. Freimuth, H. Zhang, S. Blügel, Y. Mokrousov, D. E. Bürgler, C. M. Schneider, *Phys. Rev. Lett.* **2011**, *107*, 086603.

[66] P. M. Oppeneer, in *Handbook of Magnetic Materials*, Vol. *13* (Ed: K. H. J. Buschow), Elseveier, Amsterdam, The Netherlands **2001**, pp. 229–422.

[67] Z. Fang, N. Nagaosa, K. S. Takahashi, A. Asamitsu, R. Mathieu, T. Ogasawara, H. Yamada, M. Kawasaki, Y. Tokura, K. Terakura, *Science* **2003**, *302*, 92.

[68] P. M. Oppeneer, T. Maurer, J. Sticht, J. Kübler, *Phys. Rev. B* **1992**, *45*, 10924.

[69] R. Starke, G. A. H. Schober, *Photonics Nanostruct. - Fundam. Appl.* **2015**, *14*, 1.

[70] T. Stobiecki, K. Kowalski, Z. Obuszko, *Physica B+C* **1985**, *130*, 94.

[71] M. Hartmann, T. R. Mcguire, *Phys. Rev. Lett.* **1983**, *51*, 1194.

[72] C. Stamm, C. Murer, M. Berritta, J. Feng, M. Gabureac, P. M. Oppeneer, P. Gambardella, *Phys. Rev. Lett.* **2017**, *119*, 087203.

[73] B. Cheng, Y. Wang, D. Barbalas, T. Higo, S. Nakatsuji, N. P. Armitage, *Appl. Phys. Lett.* **2019**, *115*, 012405.

[74] J. Weischenberg, F. Freimuth, J. Sinova, S. Blügel, Y. Mokrousov, *Phys. Rev. Lett.* **2011**, *107*, 106601.

[75] M. Zhu, H. Chong, Q. B. Vu, R. Brooks, H. Stamper, S. Bennett, *J. Appl. Phys.* **2016**, *119*, 073907.

[76] J. Christian, L. V. Zbarsky, M. von der Ehe, S. Wittrock, P. Peretzki, H. Schuhmann, A. Thomas, K. Rott, G. Reiss, T. H. Kim, M. Seibt, M. Münzenberg, *Mater. Trans.* **2015**, *56*, 1323.

[77] F. Radu, R. Abrudan, I. Radu, D. Schmitz, H. Zabel, *Nat. Commun.* **2012**, *3*, 715.

[78] Y. Mimura, N. Imamura, T. Kobayashi, A. Okada, Y. Kushiro, *J. Appl. Phys.* **1978**, *49*, 1208.

2007398 (10 of 10)